

IUCAA-22/2001, KSUPT-01/3 May 2001

Window Function for Non-Circular Beam CMB Anisotropy ExperimentTarun Souradeep^{1,2} and Bharat Ratra¹**ABSTRACT**

We develop computationally rapid methods to compute the window function for a cosmic microwave background anisotropy experiment with a non-circular beam which scans over large angles on the sky. To concretely illustrate these methods we compute the window function for the Python V experiment which scans over large angles on the sky with an elliptical Gaussian beam.

Subject headings: cosmic microwave background—cosmology: theory—methods: analytical—methods: data analysis

1. Introduction

Cosmic microwave background (CMB) anisotropy measurements are becoming an increasingly powerful tool for testing cosmogonies and constraining cosmological parameters. See, e.g., Subrahmanyan et al. (2000), Romeo et al. (2001), Dawson et al. (2000), and Padin et al. (2001) for recent CMB anisotropy observations, and, e.g., Ratra et al. (1997), Górski et al. (1998), Rocha et al. (1999), Gawiser & Silk (2000), Knox & Page (2000), Douspis et al. (2001), and Podariu et al. (2001) for discussions of constraints on models from the CMB anisotropy data.

Conventionally, the CMB temperature, $T(\gamma)$, is expressed as a function of angular position, $\gamma \equiv (\theta, \phi)$, on the sky via the spherical harmonic decomposition,

$$T(\gamma) = \sum_{\ell=0}^{\infty} \sum_{m=-\ell}^{\ell} a_{\ell m} Y_{\ell m}(\gamma). \quad (1)$$

The CMB spatial anisotropy in a Gaussian model³ is completely specified by its angular two-point correlation function $C(\gamma, \gamma')$, $= \langle T(\gamma)T(\gamma') \rangle$, between directions γ and γ' on the sky. In most

¹Department of Physics, Kansas State University, Manhattan, KS 66506.

²Current address: IUCAA, Post Bag 4, Ganeshkhind, Pune 411007, India.

³The simplest inflation models predict a Gaussian CMB anisotropy (see, e.g., Fischler, Ratra, & Susskind 1985) on all but the smallest angular scales. CMB anisotropy observations on quarter degree and larger angular scales appear to be Gaussian (see, e.g., Mukherjee, Hobson, & Lasenby 2000; Aghanim, Forni, & Bouchet 2001; Phillips & Kogut 2001; Park et al. 2001; Wu et al. 2001b, also see Podariu et al. 2001).

theoretical models the predicted fluctuations are statistically isotropic, $C(\gamma, \gamma') \equiv C(\gamma \cdot \gamma')$. The fluctuations can then be characterized solely by the angular spectrum C_ℓ , defined in terms of the ensemble average,

$$\langle a_{\ell m} a_{\ell' m'}^* \rangle = C_\ell \delta_{\ell\ell'} \delta_{mm'}, \quad (2)$$

and related to the correlation function through

$$\langle T(\gamma) T(\gamma') \rangle = \sum_{\ell=0}^{\infty} \frac{(2\ell+1)}{4\pi} C_\ell P_\ell(\gamma \cdot \gamma'), \quad (3)$$

where P_ℓ is a Legendre polynomial.

Typically, a CMB anisotropy experiment probes a range of angular scales characterized by a window function $W_\ell(\gamma, \gamma')$.⁴ To utilize the full information in the data one must use model anisotropy spectra (C_ℓ 's) defined over this range of angular scales. Such theoretical spectra are parameterized by cosmological parameters such as Ω_0 , h , and Ω_B in these models⁵, and by the spectrum of quantum fluctuations generated during inflation.

To use model C_ℓ 's in conjunction with CMB anisotropy data to estimate cosmological parameters one must be able to carefully model the CMB anisotropy experiment, i.e., accurately compute the window function W_ℓ . Given such a model of an experiment and a family of C_ℓ 's, one may optimize the fit to the data from the experiment either by using an (approximate) χ^2 technique (e.g., Ganga, Ratra, & Sugiyama 1996; Bond, Jaffe, & Knox 2000; Knox 1999; Rocha 1999; Lineweaver 2001; Dodelson 2000; Tegmark & Zaldarriaga 2000) or by using an exact maximum likelihood technique (e.g., Górski et al. 1995; Ganga et al. 1997, 1998; Ratra et al. 1998, 1999).

Current CMB anisotropy data is of significantly higher quality than data that was available just a few years ago. As a consequence an accurate model of an experimental W_ℓ must now account for effects that were ignored for earlier experiments. In this paper we develop computationally rapid methods that account for the non-circularity of the beam in a CMB anisotropy experiment window function at large angular separations where the curvature of the sky cannot be ignored. This must be accounted for in an experiment like Python V (Coble et al. 1999) which has an elliptical beam and samples a large enough area of the sky to prejudice use of the flat-sky approximation. While we focus here on Python V as a concrete illustrative example, our techniques are easily generalized to more complex cases (e.g., arbitrary beam shape, beam rotation, non-Gaussianity of the beam, etc.). Wu et al. (2001a) develop an alternate method to deal with the asymmetric beam of the MAXIMA-1 experiment.

⁴See www.phys.ksu.edu/~tarun/CMBwindows/wincomb/wincomb_tf.html for a discussion and tabulation of zero-lag window functions.

⁵Here Ω_0 is the nonrelativistic-mass density parameter, h is the Hubble parameter in units of $100 \text{ km s}^{-1} \text{ Mpc}^{-1}$, and Ω_B is the baryonic-mass density parameter.

In §2 we describe the general formalism for computing the window function. In the §§3–5 we develop specific computationally rapid methods for computing the window function in three different cases. The flat-sky approximation window function computation is covered in §3. In §4 we develop a general method, based on Wigner rotation functions, for computing the window function on a sphere, and describe how to numerically implement this scheme. In §5 we specialize to the case of an experiment like Python V where long scans are performed at constant elevation, and provide a computationally rapid method for evaluating the exact window function. Approximate window functions obtained using the flat-sky approximation and from retaining only the first few terms in a perturbation expansion (in non-circularity about a circular beam) of the Wigner rotation functions method (hereafter Wigner method) are compared to the exact window function in §6. We conclude in §7. In appendix A we describe our parameterization and normalization of an elliptical Gaussian beam, and also record analytic expressions for its Fourier and spherical harmonic transforms.

2. Window Function Computation Formalism

Owing to the finite angular resolution of a CMB anisotropy experiment, the temperature “measured” by the experiment at point γ_i on the sky is

$$\tilde{T}(\gamma_i) = \int d\Omega_\gamma B(\gamma_i, \gamma) T(\gamma). \quad (4)$$

Here $B(\gamma_i, \gamma)$ is the beam function that characterizes the angular dependence of the sensitivity of the apparatus around the pointing direction γ_i .

CMB anisotropy experiments that use a differencing or modulation scheme measure the difference in temperature between different points on the sky. The measured CMB temperature anisotropy in any differencing scheme (labelled below by index n) can be expressed as a weighted linear combination,

$$\Delta^{(n)}(\gamma_i) = \int d\Omega_\gamma w_i^{(n)}(\gamma) \tilde{T}(\gamma), \quad (5)$$

where $w_i^{(n)}(\gamma)$ are the weight functions. In our discussion of Python V below n corresponds to the harmonic number of cosine modulation weight functions. Instead of weights $w_i^{(n)}(\gamma)$ that are continuous functions, for Python V the weights $w_{ij}^{(n)}$ are discrete and characterize the sensitivity at γ_{ij} , the j^{th} point on the discretized chopper cycle around the pointing direction γ_i . In this case the integral in eq. (5) is replaced by a summation and we have

$$\Delta^{(n)}(\gamma_i) = \sum_{j=1}^{N_c} w_{ij}^{(n)} \tilde{T}(\gamma_{ij}) \quad (6)$$

where N_c is the number of points in the discretized chopper cycle.

The complete window function for modulation pair (n, m) , $W_\ell^{(n,m)}(\gamma_i, \gamma_j)$, accounts for the effects of both the beam function and the differencing or modulation scheme of the experiment and

is defined through the theoretical model covariance matrix

$$C_{ij}^{(n,m)} = \langle \Delta^{(n)}(\gamma_i) [\Delta^{(m)}(\gamma_j)]^* \rangle = \sum_{\ell=0}^{\infty} \frac{(2\ell+1)}{4\pi} C_\ell W_\ell^{(n,m)}(\gamma_i, \gamma_j). \quad (7)$$

It proves convenient to distinguish between the dependence of the window function on the finite angular resolution of the experimental apparatus (the beam function) and the dependence of the window function on the differencing scheme adopted for the experiment. Using eq. (6), the complete theoretical covariance matrix element $C_{ij}^{(n,m)}$ between pixels i and j on the sky can be expressed as a weighted linear sum of single beam correlation functions via

$$C_{ij}^{(n,m)} \equiv \sum_{p=1}^{N_c} \sum_{q=1}^{N_c} w_{ip}^{(n)} w_{jq}^{(m)} \langle \tilde{T}(\gamma_{ip}) \tilde{T}(\gamma_{jq}) \rangle. \quad (8)$$

We call the single beam correlation function $C^{(e)}(\gamma, \gamma') = \langle \tilde{T}(\gamma) \tilde{T}(\gamma') \rangle$, an elementary correlation function. The elementary correlation function does not depend on the differencing scheme used in the experiment but does depend on the beam function. We use $C^{(e)}$ to define what we call the (single beam) elementary window function $W_\ell^{(e)}$ via

$$C^{(e)}(\gamma_i, \gamma_j) = \sum_{\ell=0}^{\infty} \frac{(2\ell+1)}{4\pi} C_\ell W_\ell^{(e)}(\gamma_i, \gamma_j). \quad (9)$$

$W_\ell^{(e)}$ depends on the beam function of the experiment but not on the differencing strategy used. Using eqs. (8) and (9) the complete window function may be expressed as a weighted linear sum of elementary window functions via

$$W_\ell^{(n,m)}(\gamma_i, \gamma_j) = \sum_{p=1}^{N_c} \sum_{q=1}^{N_c} w_{ip}^{(n)} w_{jq}^{(m)} W_\ell^{(e)}(\gamma_{ip}, \gamma_{jq}). \quad (10)$$

Using eqs. (3), (4), and (9) the elementary window function may be expressed as

$$\begin{aligned} W_\ell^{(e)}(\gamma_i, \gamma_j) &= \int d\Omega_\gamma d\Omega_{\gamma'} B(\gamma_i, \gamma) B(\gamma_j, \gamma') P_\ell(\gamma \cdot \gamma') \\ &= \frac{4\pi}{2\ell+1} \sum_{m=-\ell}^{\ell} b_{\ell m}(\gamma_i) [b_{\ell m}(\gamma_j)]^*, \end{aligned} \quad (11)$$

where

$$b_{\ell m}(\gamma_i) = \int d\Omega_\gamma B(\gamma_i, \gamma) Y_{\ell m}^*(\gamma) \quad (12)$$

is the spherical harmonic transform of the beam function pointing at γ_i .

For some experiments the beam function is accurately circularly symmetric about the pointing direction, i.e., $B(\gamma_i, \gamma) \equiv B(\gamma_i \cdot \gamma)$. This allows a great simplification⁶ since the beam function can

⁶When the beam is pointing towards a Pole, γ_P , the coefficients in the spherical harmonic expansion of a circular beam function are $b_{\ell m}(\gamma_P) = B_\ell \sqrt{(2\ell+1)/4\pi} \delta_{m0}$. Here δ_{m0} is a Kronecker delta function and implies that the only non-zero spherical harmonic coefficients are those that result in a circularly-symmetric beam function.

then be represented as $B(\gamma_i \cdot \gamma) = (4\pi)^{-1} \sum_{\ell=0}^{\infty} (2\ell+1) B_\ell P_\ell(\gamma_i \cdot \gamma)$. Consequently, for a circularly symmetric beam function it is straightforward to derive the usual expression

$$W_\ell^{(e)}(\gamma_i, \gamma_j) = B_\ell^2 P_\ell(\gamma_i \cdot \gamma_j). \quad (13)$$

In addition to the single evaluation of the Legendre transform of the beam, B_ℓ , computation of the elementary window function for an experiment with a circular beam simply involves computing P_ℓ for all $\ell \leq \ell_{\max}$ using the stable upward recursion relation for each distinct pixel pair separation. This is computationally inexpensive (at least by a factor $\sim \ell_{\max}$) compared to the computation of the elementary window function for an experiment with arbitrary beam shape (eq. [11]).

In the next three sections we discuss three cases where one may compute the window function for an experiment with a non-circular beam in a time comparable to or just a factor of few larger than that for the same experiment assuming a circular beam. First, we consider the flat-sky approximation which is accurate if the experiment has a compact beam and the pixels are not separated by large angles (more precisely, the separation must be significantly less than a radian). This has been used previously for a number of experiments, including Python V (Coble et al. 1999; Coble 1999), MSAM (Coble 1999), and MAXIMA-1 (Wu et al. 2001a). Next, we develop a very general Wigner method that fully accounts for the curvature of the sky and accounts for the non-circularity of the beam in a perturbative expansion about a circular beam. In a case like Python V where the non-circularity of the beam is not large, the first few terms in the non-circularity perturbation expansion provide sufficient accuracy. In this case the Wigner method allows one to compute the window function in a time a factor of a few larger than that for the corresponding circular beam case. Finally, for an experiment that scans at constant elevation (such as Python V), with pixels lying on a small number of elevations, it is possible to implement a slightly different Wigner method that allows rapid computation of the exact window function for an arbitrary beam shape.

3. Window Function in the Flat-Sky Approximation

If an experiment scans a small enough patch of the sky it is computationally advantageous to work in the flat tangent plane (rather than on the sphere) and make use of Fourier transforms (rather than spherical harmonic transforms) when modeling the experiment. See, for instance, Bond & Efstathiou (1987) and Coble (1999) for discussions. We may then transform from γ to coordinates in a locally flat patch, ω , and use a two-dimensional Fourier transform approximation to the spherical harmonic transform. For instance,

$$T(\omega) = \int \frac{d^2 k}{(2\pi)^2} e^{i\mathbf{k} \cdot \omega} T(\mathbf{k}). \quad (14)$$

Here $\omega = (\omega, \phi)$, are polar coordinates in the neighborhood of the North Pole γ_P in the patch on the sky, i.e., $\gamma = \gamma_P + \omega$, or $\omega = (\omega_1, \omega_2) = (\omega \cos \phi, \omega \sin \phi)$, where $\omega = 2 \sin(\theta/2) = |\gamma - \gamma_P|$, $0 \leq$

$\omega \leq 2$, where θ is the colatitude (e.g., Bond & Efstathiou 1987). In the small-angle approximation, it may be shown that the ensemble average of the Fourier transform of the temperature

$$\langle T(\mathbf{k})T^*(\mathbf{k}') \rangle = (2\pi)^2 C_k \delta^{(2)}(\mathbf{k} - \mathbf{k}'), \quad (15)$$

where $k = |\mathbf{k}|$ and C_k is the CMB anisotropy power spectrum. This flat-sky analog of eq. (2) is obtained assuming statistical homogeneity on the flat sky. The angular correlation function can then be expressed as

$$\langle T(\boldsymbol{\omega}_i) T(\boldsymbol{\omega}_j) \rangle = \frac{1}{2\pi} \int_0^\infty dk k J_0(k|\boldsymbol{\omega}_i - \boldsymbol{\omega}_j|) C_k, \quad (16)$$

where J_0 is the zeroth order Bessel function of the first kind. Comparing this expression to that in eq. (3) in the small angular separation and large ℓ regime where $P_\ell(\cos \theta) \rightarrow J_0([\ell + 1/2]\theta)$, we arrive at the correspondence $k \sim \ell + 1/2$ between the radial wavenumber on the flat sky k and the spherical multipole ℓ .

For an experiment for which the flat-sky approximation is valid the “measured” temperature (see eq. [4]) is

$$\tilde{T}(\boldsymbol{\omega}_i) = \int \frac{d^2 k}{(2\pi)^2} e^{i\mathbf{k}\cdot\boldsymbol{\omega}_i} B(\mathbf{R}_i[\mathbf{k}]) T(\mathbf{k}), \quad (17)$$

where $B(\mathbf{k})$ is the Fourier transform of the beam function pointing at the origin $\boldsymbol{\omega} = 0$ of the local flat coordinate patch. The rotation operator \mathbf{R}_i (which rotates \mathbf{k} by an angle ϱ_i) accounts for a possible rotation of the telescope beam pointing at $\boldsymbol{\omega}_i$ relative to the telescope beam pointing at the origin. In addition to the case when the telescope physically rotates around its axis as it moves from one pointing direction to another, non-zero values of ϱ_i can arise when the telescope is not located at a Pole and also when a single flat-sky coordinate system is set up on a patch large enough for sky curvature to be important. In the latter two cases this rotation is important only in the regime where one expects the flat-sky approximation to be poor.

The modulated temperature $\Delta^{(n)}(\boldsymbol{\gamma}_i)$ expressed in terms of $\tilde{T}(\boldsymbol{\omega}_{ij})$ is given by eq. (6). The window function $W_\ell^{(n,m)}(\boldsymbol{\gamma}_i, \boldsymbol{\gamma}_j)$ is defined through the covariance matrix by

$$C_{ij}^{(n,m)} = \sum_{\ell=0}^{\infty} \frac{(2\ell + 1)}{4\pi} C_\ell W_\ell^{(n,m)}(\boldsymbol{\gamma}_i, \boldsymbol{\gamma}_j) \simeq \int_0^\infty \frac{dk}{2\pi} k C_k W_k^{(n,m)}(\boldsymbol{\gamma}_i, \boldsymbol{\gamma}_j), \quad (18)$$

where we identify the flat space radial wavenumber k with $\ell + 1/2$. The complete window function $W_k^{(n,m)}(\boldsymbol{\gamma}_i, \boldsymbol{\gamma}_j)$ may be expressed in terms of elementary window functions $W_k^{(e)}$ by using eq. (10).

Using eqs. (9) and (17), the expression for the elementary window function in the flat-sky approximation is

$$W_k^{(e)}(\boldsymbol{\omega}_i, \boldsymbol{\omega}_j) = \int_0^{2\pi} \frac{d\phi_k}{2\pi} e^{i\mathbf{k}\cdot(\boldsymbol{\omega}_i - \boldsymbol{\omega}_j)} B(\mathbf{R}_i[\mathbf{k}]) B^*(\mathbf{R}_j[\mathbf{k}]). \quad (19)$$

Further analytical manipulations are needed to derive an expression suitable for numerical evaluation. Without loss of generality, we transform to a new flat coordinate system with ω_i as the origin: $\omega'_i = (0, 0)$ and $\omega'_j = (\omega'_1, \omega'_2)$. In what follows we drop the prime on the new coordinates. For small angular separations, $\omega = |\omega_i - \omega_j| \ll 1$, we have

$$W_k^{(e)}(\omega_i, \omega_j) = \int_0^{2\pi} \frac{d\phi_k}{2\pi} \cos[k\omega \cos(\phi_k - \alpha)] B(\mathbf{k}) B^*(\mathbf{R}_j[\mathbf{k}]), \quad (20)$$

where we have defined $\alpha = \tan^{-1}(\omega_2/\omega_1)$.

For an elliptical Gaussian beam function (eq. [A1]), an analytic expression for $B(\mathbf{k})$ is given in eq. (A7). Using this in eq. (20) (and ignoring rotations, $\varrho_j = 0$) we obtain

$$W_k^{(e)}(\omega_i, \omega_j) = \int_0^\pi \frac{d\phi_k}{\pi} \cos[k\omega \cos(\phi_k - \alpha)] \exp[-k^2\sigma_1^2(1 + \varepsilon \sin^2 \phi_k)], \quad (21)$$

where σ_1 and σ_2 are the beamwidths (in radians) along the major and minor axis of the elliptical Gaussian beam. It is useful to define the RMS beamwidth $\sigma_{\text{RMS}} = \sqrt{(\sigma_1^2 + \sigma_2^2)/2}$, and a measure of the non-circularity of the elliptical beam $\varepsilon = (\sigma_2/\sigma_1)^2 - 1$.

The expression for the flat-sky window function for an elliptical Gaussian beam given in eq. (21) can be readily evaluated numerically. It can also be expressed analytically as an infinite series expansion, $W_k^{(e)} = \sum_{n=0}^{\infty} (-1)^n b_k^n {}^{(n)}W_k^{(e)}$, in powers of an anisotropy or non-circularity parameter $b_k = \varepsilon(\sigma_1 k)^2 = k^2(\sigma_2^2 - \sigma_1^2)$. The series is perturbative ($b_k < 1$) up to multipoles $\ell \lesssim |\sigma_2^2 - \sigma_1^2|^{-1/2}$, which can be considerably larger than the inverse of the RMS beamwidth σ_{RMS} . As expected, the first ($n = 0$) term in this series corresponds to the circular beam function result ($\sigma_1 = \sigma_2 = \sigma$),

$${}^{(0)}W_k^{(e)}(\omega_i, \omega_j) = J_0(k\omega) e^{-k^2\sigma_1^2}. \quad (22)$$

For a non-circular Gaussian beam function the next few terms are

$${}^{(1)}W_k^{(e)}(\omega_i, \omega_j) = \left[\frac{J_1(k\omega)}{k\omega} - J_2(k\omega) \sin^2 \alpha \right] e^{-k^2\sigma_1^2} \quad (23)$$

$${}^{(2)}W_k^{(e)}(\omega_i, \omega_j) = \frac{1}{2} \left[3 \frac{J_2(k\omega)}{(k\omega)^2} - 6 \frac{J_3(k\omega)}{k\omega} \sin^2 \alpha + J_4(k\omega) \sin^4 \alpha \right] e^{-k^2\sigma_1^2}, \quad (24)$$

where $J_m(x)$ is the m^{th} order Bessel function of the first kind. At arbitrary order n the term is

$$\begin{aligned} {}^{(n)}W_k^{(e)}(\omega_i, \omega_j) = & \frac{\sqrt{\pi} \Gamma(n + 1/2)}{\Gamma(n + 1)} e^{-k^2\sigma_1^2} \sum_{m=0}^n \frac{(\sin \alpha)^{2m} (\cos \alpha)^{2(n-m)}}{\Gamma(n-m+1) \Gamma(m+1)} \\ & \times {}_1F_2 \left[\frac{1}{2} + m, \left(\frac{1}{2}, 1+n \right), -\frac{(k\omega)^2}{4} \right], \end{aligned} \quad (25)$$

where Γ is the Euler gamma function and ${}_1F_2$ is a generalized hypergeometric function. Figure 1 shows contour plots of the zeroth order (eq. [22]) and first order (eq. [23]) terms in the non-circularity expansion of the flat-sky window function. These are computed for parameter values characterizing the Python V experiment (see §6 below for details of the experiment).

4. Wigner Method Window Function

If an experiment takes data over a large enough area of the sky the formalism developed in the previous section, based on the flat-sky approximation, cannot be used to compute the window function. In this section we develop a general method for computing the window function for an experiment with an arbitrary beam shape that collects data from a large area on the sky.

For pointing direction $\gamma_i = (\theta_i, \phi_i)$, and vector in the beam $\gamma = (\theta, \phi)$, the beam function may be expanded in a spherical harmonic decomposition,

$$B(\gamma_i, \gamma) = \sum_{\ell=0}^{\infty} \sum_{m=-\ell}^{\ell} b_{\ell m}(\gamma_i) Y_{\ell m}(\gamma). \quad (26)$$

Here the expansion coefficients, $b_{\ell m}$, are given by eq. (12).

For ease of computation it is convenient to rotate to a new coordinate system in which the new \mathbf{x}'_3 axis lies along the pointing direction γ_i . This is accomplished by first rotating the coordinate system around the \mathbf{x}_3 axis by ϕ_i and then rotating around the new \mathbf{x}'_2 axis by θ_i . Then

$$B(\mathbf{x}'_3, \gamma') = \sum_{\ell'=0}^{\infty} \sum_{m'=-\ell'}^{\ell'} b_{\ell' m'}(\mathbf{x}'_3) Y_{\ell' m'}(\gamma') = B(\gamma_i, \gamma), \quad (27)$$

where the last step follows from the fact that B is a scalar.

If the experiment is not located at a Pole, the beam of a telescope which does not rotate around its beam axis will, nevertheless, appear to “rotate” around the beam axis with respect to the local azimuth and declination directions. We hence allow for a rotation ϱ_i of the beam around the beam axis relative to a parallel transport of the beam on the sky from the Pole $\gamma'_P = \mathbf{x}'_3$, to the pointing direction γ'_i . The Python V experiment was located at the South Pole and hence has $\varrho_i = 0$. The rotation ϱ_i can also account for non-circular beam function cases where the telescope rotates around its axis as it moves from one pointing direction to another (e.g., one mounted on a satellite).

The rotations of the previous two paragraphs correspond to Euler angles $\alpha = \phi_i$, $\beta = \theta_i$, and $\gamma = \varrho_i$ in the notation of Scheme A of §14.1 of Varshalovich, Moskalev, & Khersonskii (1988, hereafter VMK). From eq. (1) of their §5.5.1 we have

$$Y_{\ell' m'}(\gamma') = \sum_{m''=-\ell'}^{\ell'} Y_{\ell' m''}(\gamma) D_{m'' m'}^{\ell'}(\phi_i, \theta_i, \varrho_i), \quad (28)$$

where $D_{m'' m'}^{\ell'}$ is a Wigner D -function corresponding to the rotation of the beam. From eqs. (28) and (27) we have

$$b_{\ell m}(\gamma_i) = \sum_{m'=-\ell}^{\ell} b_{\ell m'}(\mathbf{x}'_3) D_{m m'}^{\ell}(\phi_i, \theta_i, \varrho_i). \quad (29)$$

We focus on the elementary window function, i.e., ignore the modulation and consider the window function for two points γ_i and γ_j (see eq. [11]). Using the usual decomposition for the Legendre polynomial in terms of spherical harmonics, the fact that B is real, and eqs. (28) and (29), we find

$$\begin{aligned} W_\ell^{(e)}(\gamma_i, \gamma_j) &= \frac{4\pi}{2\ell+1} \sum_{m'=-\ell}^{\ell} \sum_{m''=-\ell}^{\ell} [b_{\ell m'}(\mathbf{x}'_3)]^* b_{\ell m''}(\mathbf{x}'_3) \\ &\quad \times \sum_{m=-\ell}^{\ell} [D_{mm'}^\ell(\phi_i, \theta_i, \varrho_i)]^* D_{mm''}^\ell(\phi_j, \theta_j, \varrho_j). \end{aligned} \quad (30)$$

When the beam function is circularly symmetric $b_{\ell m}(\mathbf{x}'_3) = \delta_{m0} B_\ell \sqrt{2\ell+1}$. Using $D_{m0}^\ell(\theta, \phi, \varrho) = Y_{\ell m}(\theta, \phi)$, it is straightforward to establish that in this case eq. (30) reduces to the usual expression given in eq. (13).

Using the addition theorem for Wigner D -functions (eqs. [2] of §4.4, [1] of §4.3, and [5] and [6] of §4.7.2 of VMK), we reduce eq. (30) to the simpler form,

$$W_\ell^{(e)}(\gamma_i, \gamma_j) = \frac{4\pi}{2\ell+1} \sum_{m'=-\ell}^{\ell} \sum_{m''=-\ell}^{\ell} [b_{\ell m'}(\mathbf{x}'_3)]^* b_{\ell m''}(\mathbf{x}'_3) D_{m'm''}^\ell(\alpha - \varrho_i, \gamma, \beta + \varrho_j), \quad (31)$$

where

$$\begin{aligned} \cos\gamma &= \cos\theta_i \cos\theta_j + \sin\theta_i \sin\theta_j \cos(\phi_i - \phi_j) = \gamma_i \cdot \gamma_j \\ \cot\alpha &= -\cos\theta_i \cot(\phi_i - \phi_j) + \sin\theta_i \cot\theta_j \csc(\phi_i - \phi_j) \\ \cot\beta &= -\cos\theta_j \cot(\phi_i - \phi_j) + \cot\theta_i \sin\theta_j \csc(\phi_i - \phi_j). \end{aligned} \quad (32)$$

For large values of ℓ it is computationally expensive to evaluate the entire m' and m'' sum in eq. (31). However, for a smooth, mildly non-circular beam function (defined precisely below), restricting the summation to a few low values of m' and m'' results in a good approximation. A smooth (i.e., not sharply peaked) beam function results in $b_{\ell 0}$ falling off with increasing ℓ . At large ℓ and small γ , $D_{mm'}^\ell(\alpha, \gamma, \beta) \rightarrow e^{-im\alpha-im'\beta} J_{|m-m'|}([\ell+1/2]\gamma)$. Thus the $D_{m'm''}^\ell$ term in eq. (31) strongly suppresses, as $(\ell\gamma)^{|m'-m''|}$, the contribution from off-diagonal $m' \neq m''$ terms. In addition, mild non-circularity requires that at each value of ℓ the ratio $|b_{\ell m}/b_{\ell 0}|$ decrease rapidly with increasing $|m|$. Hence the products $b_{\ell m'}^* b_{\ell m''}$, as functions of ℓ , are ordered in magnitude and fall off as one goes to higher values of $|m'| + |m''|$. For Python V where the deviation from circularity is small, retaining the first non-zero order term is sufficient for computing an accurate covariance function.⁷

⁷By a sufficiently accurate covariance function we mean that the maximum likelihood analysis results are not significantly affected by higher order corrections. This criterion of sufficient accuracy therefore depends on the level of noise in the experiment, which is encoded in the noise covariance matrix of the experiment.

We now derive explicit expressions for the first few leading order terms in eq. (31) for the specific case of an elliptical beam function. For an elliptical beam function, symmetry dictates that $b_{\ell m}(\mathbf{x}'_3) = 0$ for odd m (see appendix A). In what follows beam rotations are set to zero ($\varrho_i = 0$), but it is straightforward to restore them from the complete expression given above. The zeroth order term contains D_{00}^ℓ , the first order term has four contributors (D_{02}^ℓ , $D_{0,-2}^\ell$, D_{20}^ℓ , and $D_{-2,0}^\ell$), and the second order term has eight contributors (D_{22}^ℓ , $D_{2,-2}^\ell$, $D_{-2,2}^\ell$, $D_{-2,-2}^\ell$, D_{04}^ℓ , $D_{0,-4}^\ell$, D_{40}^ℓ , and $D_{-4,0}^\ell$).

After a significant amount of algebraic manipulations (that use equations from §§4.3, 4.4, 4.8, and 4.17 of VMK, familiar properties of Legendre polynomials and modified Bessel functions, and the reality condition on the beam, eq. [A8]), we find a series expansion of the elementary window function,

$$W_\ell^{(e)}(\gamma_i, \gamma_j) = \frac{4\pi}{2\ell+1} \left[\begin{aligned} & [b_{\ell 0}(\mathbf{x}'_3)]^2 d_{00}^\ell(\gamma) + 2b_{\ell 0}(\mathbf{x}'_3)b_{\ell 2}(\mathbf{x}'_3) \{ \cos(2\alpha) + \cos(2\beta) \} d_{02}^\ell(\gamma) \\ & + 2[b_{\ell 2}(\mathbf{x}'_3)]^2 \left[\cos(2\alpha + 2\beta) d_{22}^\ell(\gamma) + (-1)^{-\ell} \cos(2\alpha - 2\beta) d_{22}^\ell(\pi - \gamma) \right] \\ & + 2b_{\ell 0}(\mathbf{x}'_3)b_{\ell 4}(\mathbf{x}'_3) \{ \cos(4\alpha) + \cos(4\beta) \} d_{04}^\ell(\gamma) + \dots \end{aligned} \right]. \quad (33)$$

Here the angles α , β , and γ are defined in eqs. (32), and the $d_{mm'}^\ell$'s are the usual Wigner d -functions of angular momentum theory (e.g., §4.3 of VMK) related to the Wigner D -functions through $D_{mm'}^\ell(\alpha, \gamma, \beta) = e^{-im\alpha} d_{mm'}^\ell(\gamma) e^{-im'\beta}$. More precisely,

$$\begin{aligned} d_{00}^\ell(\gamma) &= P_\ell(\cos\gamma), \\ d_{02}^\ell(\gamma) &= -\sqrt{\frac{\ell(\ell+1)}{(\ell-1)(\ell+2)}} P_\ell(\cos\gamma) + \frac{2\cos\gamma}{\sqrt{(\ell-1)\ell(\ell+1)(\ell+2)}} P'_\ell(\cos\gamma), \\ d_{22}^\ell(\gamma) &= \frac{1}{(\ell-1)(\ell+2)} \left[-4 \left(\frac{2-\cos\gamma}{1+\cos\gamma} \right) + \ell(\ell+1) \right] P_\ell(\cos\gamma) \\ &+ \frac{4(1-\cos\gamma)}{(\ell-1)\ell(\ell+1)(\ell+2)} \left[- \left(\frac{2-\cos\gamma}{1+\cos\gamma} \right) + \ell(\ell+1) \right] P'_\ell(\cos\gamma), \\ d_{22}^\ell(\pi - \gamma) &= \frac{(-1)^\ell}{(\ell-1)(\ell+2)} \left[-4 \left(\frac{2+\cos\gamma}{1-\cos\gamma} \right) + \ell(\ell+1) \right] P_\ell(\cos\gamma) \\ &+ \frac{4(-1)^{\ell+1}(1+\cos\gamma)}{(\ell-1)\ell(\ell+1)(\ell+2)} \left[- \left(\frac{2+\cos\gamma}{1-\cos\gamma} \right) + \ell(\ell+1) \right] P'_\ell(\cos\gamma), \\ d_{04}^\ell(\gamma) &= -\ell(\ell+1) \sqrt{\frac{(\ell-4)!}{(\ell+4)!}} \left[\frac{6(1+3\cos^2\gamma)}{\sin^2\gamma} - \ell(\ell+1) \right] P_\ell(\cos\gamma) \\ &+ 8\sqrt{\frac{(\ell-4)!}{(\ell+4)!}} \cos\gamma \left[\frac{3(1+\cos^2\gamma)}{\sin^2\gamma} - \ell(\ell+1) \right] P'_\ell(\cos\gamma), \end{aligned} \quad (34)$$

where $P'_\ell \equiv dP_\ell(x)/dx$. Recursion relations in the indices ℓ , m and m' (see VMK) can be used to compute $d_{mm'}^\ell$ for larger values of m and m' .

Evaluating the first few terms of the Wigner method expansion in eq. (33) involves computing P_ℓ and P'_ℓ . The first derivative P'_ℓ can be readily computed in terms of P_ℓ and $P_{\ell-1}$ during the generation of P_ℓ using the upward recursion relation. Hence the computational cost of evaluating $W_\ell^{(e)}$ for a mildly non-circular beam function (using eq. [33]) is only a factor of a few larger than that for a circular beam function.

Figure 2 shows, as a function of $\ell\sigma_{\text{RMS}}$, the six leading order $|b_{\ell m}(\mathbf{x}'_3) b_{\ell m'}(\mathbf{x}'_3)|$ coefficients (with $m, m' = 0, 2, 4$) of the expansion of eq. (31) (see eq. [33]) for the Python V experiment. These are also the leading order contributors to the zero-lag elementary window function. Note that the curves do not cross at any ℓ , i.e., the ordering of the coefficients is maintained for all ℓ , and at large ℓ (past the peak) higher order terms fall off more rapidly with ℓ . Hence this perturbation expansion is an efficient scheme for computing non-circularity corrections. The non-circularity corrections peak at angular scales smaller than the RMS beamwidth σ_{RMS} . Thus non-circularity corrections are not that important for an elementary window function (a single beam experiment) but can have a significant effect on the complete window function for a modulated experiment if the modulation scheme results in sensitivity to the $\ell\sigma_{\text{RMS}} > 1$ regime.

Figure 3 shows contour plots of the isotropic term $d_{00}^\ell(\gamma)$ and the leading order correction term $\{\cos(2\alpha) + \cos(2\beta)\} d_{02}^\ell(\gamma)$ in the perturbation expansion of the Wigner method elementary window function (see eq. [33]) for the Python V experiment. These are plotted for multipole $\ell = 100$ chosen so that $\ell\sigma_{\text{RMS}} \sim 1$, which is where the non-circularity correction starts becoming significant. Close to the center of the plots this non-circularity correction is larger along the major and minor axes of the elliptical beam. The correction term falls off with increasing pixel separation, suggesting that the circular beam function approximation is good for sufficiently large separations. Also, for a modestly non-circular beam function this implies that higher order terms in the Wigner method perturbation expansion need be retained only for close pixel pairs and one can hence truncate the summation in eq. (31) at lower orders for progressively more widely separated pixel pairs.

5. Constant Elevation Scan Window Function

For an experiment, such as Python V, that scans at constant elevation⁸, it is possible to derive another expression for the window function which does not require use of the approximation of the previous section (the truncation of the m' and m'' series).

We follow the initial development of the previous section and transform to a new coordinate system by rotating around the \mathbf{x}_3 axis by ϕ_i , where $\boldsymbol{\gamma}_i = (\theta_i, \phi_i)$ is the pointing direction. The Euler angles of this rotation are $\alpha = \phi_i$, $\beta = 0$, and $\gamma = \varrho_i$. As described in the previous section, ϱ_i represents a relative rotation of the beam around its axis. For an experiment located at one of

⁸Constant elevation here refers most generally to any set of parallel circles on the sky.

the Poles $\varrho_i = 0$. In general, we have

$$b_{\ell m}(\gamma_i) = \sum_{m'=-\ell}^{\ell} b_{\ell m'}(\mathbf{x}'_3) D_{mm'}^{\ell}(\phi_i, 0, \varrho_i). \quad (35)$$

From §4.16 of VMK we find $D_{mm'}^{\ell}(\phi_i, 0, \varrho_i) = e^{-im(\phi_i+\varrho_i)} \delta_{mm'}$. Equation (35) then implies $b_{\ell m}(\theta_i, \phi_i) = e^{-im(\phi_i+\varrho_i)} b_{\ell m}(\theta_i, 0)$ and so eq. (30) reduces to

$$W_{\ell}^{(e)}(\gamma_i, \gamma_j) = \frac{4\pi}{2\ell+1} \sum_{m=-\ell}^{\ell} e^{-im[(\phi_i-\phi_j) + (\varrho_i-\varrho_j)]} b_{\ell m}^*(\theta_i, 0) b_{\ell m}(\theta_j, 0). \quad (36)$$

Window functions between pixels lying on a few constant elevation lines can be rapidly computed by using eq. (36) and pre-computed $b_{\ell m}(\theta_i, 0)$'s.

For an experiment like Python V whose beam function has the symmetry $B(\theta_i, 0; \theta, \phi) = B(\theta_i, 0; \theta, -\phi)$, it may be shown that eqs. (12) and (26) and the fact that the beam function B is real implies that $b_{\ell m}(\theta_i, 0)$ is real. In this case eq. (36) may be re-expressed as

$$W_{\ell}^{(e)}(\gamma_i, \gamma_j) = \frac{4\pi}{2\ell+1} \sum_{m=-\ell}^{\ell} \cos[m\{(\phi_i - \phi_j) + (\varrho_i - \varrho_j)\}] b_{\ell m}(\theta_i, 0) b_{\ell m}(\theta_j, 0). \quad (37)$$

Here $b_{\ell m}(\theta, 0)$ is defined in the usual way through eq. (12). For the Python V experiment, which chops at constant elevation and where the pixels lie on a relatively small number of elevations⁹, it is possible to pre-compute and store the $b_{\ell m}(\theta, 0)$ at all elevations θ . Given these pre-computed $b_{\ell m}$'s, the elementary window function can be computed very rapidly by using eq. (37).

6. Comparison of Approximate and Exact Python V Covariance Matrices

Python V is a CMB anisotropy experiment which performs wide-angle scans with a non-circular beam. In this section we compare Python V window functions and theoretical covariance matrices computed in the flat-sky approximation and in the Wigner method perturbative approximation as well as in the exact method.

Python V observations were made at 37–45 GHz. Two regions of the sky were observed: the main field, a rectangle 7.5° in declination ($\delta = -52^{\circ}$ to -45°) by 67.7° in azimuth (centered on $\alpha = 23^{\text{h}}18^{\text{m}}$); and another rectangular patch 3° in declination ($\delta = -63^{\circ}$ to -60°) by 30° in azimuth (centered on $\alpha = 3^{\text{h}}0^{\text{m}}$). For detailed descriptions of the experiment and data see Coble et al. (1999) and Coble (1999).

The Python V beam function is well described by an elliptical Gaussian with FWHM beam-widths of $1^{\circ}02^{+0^{\circ}03}_{-0^{\circ}01}$ in elevation and $0^{\circ}91^{+0^{\circ}03}_{-0^{\circ}01}$ in azimuth (one standard deviation uncertainties).

⁹The 690 sky pixels of Python V lie on 11 distinct elevations.

The Python V beam function is a compact elliptical Gaussian, eq. (A1), with $\sigma_1 = 0.0076$ and $\sigma_2 = 0.0067$ as the nominal beamwidths in radians. Python V uses a constant-elevation smooth scan sampling strategy around every pixel on the sky, with a chopper throw (end to end) of $\Phi_c = 17^\circ 06$. Each chopper cycle consists of 128 time samples suitably modulated in time to correspond to the spatial modulations described below. To compute the window function we only need to know the final spatial modulation strategy adopted. See Coble (1999) for a more detailed discussion of these procedures. The constant elevation scans are discretely resampled in space (with nine-fold oversampling) at $N_c = 567$ equi-spaced points (θ_i, ϕ_i^p) labelled by integers $p = 1, 2, \dots, N_c$ along the chopper cycle around the pixel $\gamma_i = (\theta_i, \phi_i)$. The azimuth $\phi_i^p = \phi_i + (p-1)\Delta\phi + (\Phi_o - \Phi_c/2)$, where $\Delta\phi = \Phi_c/(N_c - 1)$ is the spacing between points and $\Phi_o = 0^\circ 58$ accounts for the offset between the azimuth of the pixel, ϕ_i , and the center of scan. The scans are modulated using the first eight cosine harmonics of the chopper cycle (hereafter modulations 1 to 8). All modulations, other than the first, are apodized by a Hann window to reduce ringing in multipole space and down weight data taken during chopper turnaround. For the modulated Python V scans the weight functions (see eq. [6]) are¹⁰

$$w_{ip}^{(m)} = \frac{2M_p^{(m)}}{\sum_{p=1}^{N_c} |M_p^{(m)}|} \quad (38)$$

where

$$\begin{aligned} M_p^{(1)} &= \cos(2\pi Z_p) \\ M_p^{(m)} &= \frac{(-1)^{m+1}}{2} \cos(2\pi m Z_p) [1 - \cos(2\pi Z_p)], \quad (m > 1) \end{aligned} \quad (39)$$

with $Z_p = (p-1)/(N_c - 1)$. These weights are used to obtain the Python V complete window function $W_\ell^{(n,m)}(\gamma_i, \gamma_j)$ (between modulation m of the scan around sky pixel γ_i and modulation n of the scan around sky pixel γ_j) in terms of the elementary window functions (see eq. [10]).

The $M_p^{(m)}$ are identical for all pixels hence $w_{ip}^{(m)}$ is independent of pixel index i . With identical constant-elevation chops around every pixel, eq. (10) can be re-expressed in a computationally more efficient form. In this case the elementary window function $W_\ell^{(e)}$ depends only on $\phi_i^p - \phi_j^q$ (at fixed θ_i and θ_j). This reduces the number of separations at which $W_\ell^{(e)}$ is needed and thus speeds up the computation. In this case we may re-express the window function as

$$\begin{aligned} W_\ell^{(n,m)}(\gamma_i, \gamma_j) = & \sum_{q_1=1}^{N_c-1} \sum_{q_2=1}^{N_c-q_1} \left[w_{i(q_2+q_1)}^{(n)} w_{j(q_2+q_1)}^{(m)} W_\ell^{(e)}(\theta_i, \theta_j, \phi_i - \phi_j + q_1 \Delta\phi) \right. \\ & \left. + w_{iq_2}^{(n)} w_{j(q_2+q_1)}^{(m)} W_\ell^{(e)}(\theta_i, \theta_j, \phi_i - \phi_j - q_1 \Delta\phi) \right] \end{aligned}$$

¹⁰The following expressions correct a typographical error in the corresponding expressions in Coble et al. (1999) and Coble (1999).

$$+ \sum_{q_2=1}^{N_c-1} w_{iq_2}^{(n)} w_{jq_2}^{(m)} W_\ell^{(e)}(\theta_i, \theta_j, \phi_i - \phi_j). \quad (40)$$

Here the three arguments of the elementary window functions (the three $W_\ell^{(e)}$ between two directions) are the colatitudes of the two directions and the difference in their azimuth angles. Pre-computing the second summations over the weight products, $\varpi_p^{(m,n)} = \sum_{q=1}^{N_c-p} w_{i(q+p)}^{(n)} w_{jq}^{(m)}$, for the set of all the modulation pairs speeds up the evaluation of the right hand side of eq. (40).

Figure 4 shows the eight equal-modulation exact Python V zero-lag complete window functions at the two extreme values of the declination, $\delta = -63^\circ$ and $\delta = -45.4^\circ$. Also plotted for comparison is the zero-lag elementary window function at $\delta = -63^\circ$. The effect of beam function non-circularity is more pronounced for the modulated (complete) window functions since these have peak sensitivity at multipoles well beyond the inverse beamwidth, which is where the non-circularity corrections start to become important (see Fig. 2).

While it is of interest to estimate the accuracy of window functions computed in various approximations, the accuracy of computed covariance matrix elements is of much greater relevance since these directly determine the accuracy of cosmological results extracted from CMB anisotropy data. This significantly extends the range of usefulness of approximate window functions. First, the sum over ℓ in the definition of the theoretical model covariance matrix, eq. (7), averages over and hence reduces the significance of deviations between the approximate and exact window functions. For example, an approximate window function that has large deviations from the exact window function only in regimes where they oscillate in ℓ may still result in an accurate covariance matrix. Second, errors in the window function are unimportant when the corresponding covariance matrix elements are small (subdominant). For example, while the flat-sky approximation window function is very inaccurate for a widely separated pixel pair, the covariance matrix element for such a pixel pair is subdominant and thus cannot significantly influence the results from a maximum likelihood analysis of the data. Another important consideration is the level of noise in the experiment. Since the inverse of the sum of the theoretical model and noise covariance matrices, $(C_T + C_N)^{-1}$, determines the results of the maximum likelihood analysis, the model covariance matrix needs to be computed to higher accuracy for an experiment with lower noise.

Equation (7) defines the model covariance matrix element $C_{ij}^{(m,n)}$ in terms of the window function and the model CMB anisotropy power spectrum. To compare covariance matrices computed using different approximations therefore requires choice of a model C_ℓ . We use the flat bandpower spectrum, $C_\ell \propto 1/\ell(\ell+1)$, for this purpose in what follows. With this choice of power spectrum, the quantity

$$F_\ell^{(n,m)}(\gamma_i, \gamma_j) = \sum_{\ell'=2}^{\ell} \frac{2\ell'+1}{\ell'(\ell'+1)} W_{\ell'}^{(n,m)}(\gamma_i, \gamma_j), \quad (41)$$

is a measure of the cumulative build up of the corresponding covariance matrix element as one progresses with the sum over multipole ℓ in eq. (7). Up to a multiplicative normalization constant, $F_\ell^{(n,m)}(\gamma_i, \gamma_j)$ converges to the covariance matrix $C_{ij}^{(n,m)}$ as $\ell \rightarrow \infty$. Unlike W_ℓ , F_ℓ measures ℓ -space

information that may be directly used to estimate the accuracy of the computed covariance matrix. It also allows one to determine the value of ℓ to which one must compute to achieve a desired accuracy.

Figure 5 compares Python V flat bandpower covariance matrix elements computed using the different approximations developed above. The upper panels, *a*) and *b*), show comparisons of zero-lag covariance matrix elements.¹¹ At zero-lag the flat-sky approximation is more accurate than the zeroth order (circular beam) and first order (wig20) Wigner method perturbation expansion approximations. The Wigner method gets progressively more efficient (i.e., one needs to retain fewer terms in the perturbation expansion series to achieve the desired accuracy) for non-zero-lag covariance matrix elements between increasingly separated pixels. For covariance matrix elements between very widely separated pixels even the circular beam (zeroth order) approximation suffices. The Wigner method is more accurate for lower modulations which probe lower values of ℓ where beam non-circularity corrections are smaller (see Fig. 5). The flat-sky approximation is accurate at small separations (e.g., at zero-lag). For Python V the flat-sky approximation is more accurate for pixels separated in azimuth than for pixels separated in declination. The flat-sky approximation works better for higher modulations which probe larger values of ℓ . The F_ℓ curves for the circular beam approximation (wig00) in the lower left panel *c*) also highlights the possible pitfall of not computing to large enough ℓ . Here $F_{\ell ij}$ does not converge to C_{ij} until $\ell \gtrsim 500 \sim 4\sigma_{\text{RMS}}^{-1}$.

7. Conclusion

We develop computationally rapid methods to compute the window function for a long-scan arbitrary beam shape CMB anisotropy experiment. We use these methods to compute the window function for the elliptical Gaussian beam Python V experiment.

It proves convenient to separate effects due to the modulation scheme adopted and the shape of the beam function by expressing the complete window function as a weighted sum of single-beam elementary window functions, eq. (10).

Using eq. (11) to obtain exact elementary window function for a non-circular beam experiment requires accurate computation of the spherical harmonic transform of the beam function at each pointing direction. For an experiment with a large number of pointing directions this is computationally prohibitive. For instance, Python V has 690 pixels and the scan around each is resampled at 567 points which results in ≈ 0.4 million pointing directions. Fortunately, the 690 pixels lie on only 11 distinct elevations and the scans are performed at constant elevation. Hence pre-computing and storing the spherical harmonic beam function transforms at these 11 declinations allows for rapid computation of the exact Python V window function.

¹¹Modulated zero-lag complete window functions receive contributions from non-zero-lag elementary window functions between pixels separated by as much as the chopper throw $\Phi_c = 17^\circ 06$.

In the absence of such a simplification due to a symmetry, the Wigner method perturbation expansion scheme allows an accurate computation of the window function with computational effort within a factor of a few of the corresponding computation for the case of a circular beam function. This factor depends on the order to which the perturbative expansion (about the circular beam approximation) needs to be developed to achieve the desired accuracy. In this implementation, the Wigner method requires pre-computation and storage of one spherical harmonic transform of the beam pointing at a Pole, $b_{\ell m}(\gamma_P)$. If the beam is mildly non-circular then for all ℓ $|b_{\ell m}(\gamma_P)|/|b_{\ell 0}(\gamma_P)|$ falls off rapidly with increasing $|m|$, allowing for a fast and accurate transform and simpler storage. In the Appendix we record a semi-analytic expression for the beam function transform for a compact elliptical Gaussian beam. In mildly non-circular cases, such as Python V, $|b_{\ell m}(\gamma_P)|/|b_{\ell 0}(\gamma_P)| \rightarrow 0$ rapidly with increasing $|m|$ and the first order Wigner method is sufficiently accurate. We also develop a flat-sky approximation for window function computation and illustrate this method by computing the Python V window function.¹² We find that the flat-sky approximation works well at zero-lag and for pixels at small constant-elevation separation. At larger separations the Wigner method is more accurate than the flat-sky approximation.

The methods developed in this paper are easily extended to other cases not explicitly considered here (such as a non-circular non-Gaussian beam, a beam that rotates on the sky, etc.). Elsewhere we summarize an analysis of the Python V data that makes use of these methods.

We acknowledge very valuable discussions with K. Coble, advice from S. Dodelson, M. Draganov, K. Ganga, L. Knox, and the rest of the Python collaboration, and support from NSF CAREER grant AST-9875031.

A. Elliptical Gaussian Beam Function: Normalization & Transforms

Python V is an example of an experiment with a compact elliptical Gaussian beam function (Coble et al. 1999). In such a case it is possible to obtain accurate and useful semi-analytic expressions for the Fourier transform $B(\mathbf{k})$ and the spherical harmonic transform $b_{\ell m}(\gamma_P)$ of the beam function.

An elliptical Gaussian beam function that is compact enough can be expressed, in a locally flat-sky coordinate system (around the beam pointing direction), as

$$B(\mathbf{x}) = \frac{1}{2\pi\sigma_1\sigma_2} \exp \left[-\frac{x_1^2}{2\sigma_1^2} - \frac{x_2^2}{2\sigma_2^2} \right]. \quad (\text{A1})$$

Here $\mathbf{x} = (x_1, x_2)$ are locally flat-sky cartesian coordinates and σ_1 and σ_2 are the beamwidths in

¹²Our flat-sky approximation differs from that implemented in Coble et al. (1999) and Coble (1999).

the \mathbf{x}_1 and \mathbf{x}_2 directions.¹³ It is straightforward to establish that this is normalized so that

$$\int_{-\infty}^{\infty} dx_1 \int_{-\infty}^{\infty} dx_2 B(\mathbf{x}) = 1. \quad (\text{A2})$$

We shall have need for the expression for the beam in local spherical polar coordinates $\boldsymbol{\gamma} = (\theta, \phi)$, around the pointing direction which, without loss of generality, can be assumed to be the North Pole $\boldsymbol{\gamma}_P$. To fix the orientation of the beam on the sky we choose x_1 to lie along $\phi = 0$. Using the local mapping, $x_1 = \theta \cos \phi$ and $x_2 = \theta \sin \phi$, we can write

$$B(\boldsymbol{\gamma}_P, \boldsymbol{\gamma}) = \frac{1}{2\pi\sigma_1\sigma_2} \exp \left[-\frac{\theta^2}{2\sigma^2(\phi)} \right], \quad (\text{A3})$$

where the “beamwidth” is a function of the polar angle

$$\sigma^2(\phi) = \frac{\sigma_1^2}{1 + \epsilon^2 \sin^2 \phi}, \quad (\text{A4})$$

and a non-circularity parameter

$$\epsilon = \frac{\sigma_1^2 - \sigma_2^2}{\sigma_2^2}. \quad (\text{A5})$$

With the usual accurate approximation, allowed by the rapid fall off of the Gaussian in θ in eq. (A3), it is straightforward to establish that the normalization condition

$$\int_0^{2\pi} d\phi \int_0^\pi d\theta \sin \theta B(\boldsymbol{\gamma}_P, \boldsymbol{\gamma}) = 1 \quad (\text{A6})$$

is satisfied for $\sigma(\phi) \ll 1$.

In the flat-sky approximation the elementary window function defined in eq. (19) depends on the Fourier transform of the beam function $B(\mathbf{k})$. For the elliptical Gaussian beam function of eq. (A1) we find

$$B(\mathbf{k}) = \exp \left[-\frac{k_1^2 \sigma_1^2}{2} - \frac{k_2^2 \sigma_2^2}{2} \right]. \quad (\text{A7})$$

One great advantage of the flat-sky approximation is that Fast Fourier Transform techniques may be used to rapidly compute $B(\mathbf{k})$ for any beam function.

To use eq. (31) to compute the curved-sky window function we need to compute the spherical harmonic transform $b_{\ell m}(\boldsymbol{\gamma}_P)$ of the beam function pointed at the North Pole $\boldsymbol{\gamma}_P$. An elliptical Gaussian beam function results in a semi-analytic expression that requires numerical evaluation of only a single integral. A more complex beam function could require a complete numerical analysis.

We first note that it is straightforward to show that

$$[b_{\ell m}(\boldsymbol{\gamma})]^* = (-1)^m b_{\ell, -m}(\boldsymbol{\gamma}). \quad (\text{A8})$$

¹³The beam function is also a function of the pointing direction \mathbf{x}_0 , $B(\mathbf{x}_0, \mathbf{x})$, taken to be at the origin here.

From eqs. (A3) and (12) we find

$$b_{\ell m}(\gamma_P) = \frac{(-1)^{-m}}{2\pi\sigma_1\sigma_2} \sqrt{\frac{2\ell+1}{4\pi} \frac{(\ell+m)!}{(\ell-m)!}} \int_0^{2\pi} d\phi e^{-im\phi} \int_0^\pi d\theta \sin\theta e^{-\theta^2/[2\sigma^2(\phi)]} P_\ell^{-m}(\cos\theta), \quad (\text{A9})$$

where we have used the usual expression for $Y_{\ell m}^*$ in terms of the associated Legendre function P_ℓ^{-m} . For a compact beam, and for large ℓ , the θ integral may be performed using the usual small- θ approximation,

$$\lim_{\ell \rightarrow \infty} \ell^m P_\ell^{-m}(\cos\theta) = J_m([\ell + 0.5]\theta), \quad (\text{A10})$$

e.g., eq. (8.722.2) of Gradshteyn & Ryzhik (1994). Using eq. (6.631.7) of Gradshteyn & Ryzhik (1994) we find

$$\begin{aligned} b_{\ell m}(\gamma_P) &= \frac{(-\ell)^{-m}}{\pi(\ell + 0.5)^{3/2}} \sqrt{\frac{(\ell+m)!}{(\ell-m)!}} \frac{1}{\sigma_1\sigma_2} \\ &\times \int_0^{2\pi} d\phi e^{-im\phi} f^3(\phi) e^{-f^2(\phi)} [I_{(m-1)/2}(f^2(\phi)) - I_{(m+1)/2}(f^2(\phi))], \end{aligned} \quad (\text{A11})$$

where I_ν is the modified Bessel function and

$$f(\phi) = \frac{(\ell + 0.5)\sigma(\phi)}{2}. \quad (\text{A12})$$

Equation (A11) is valid for $m \geq 0$; for $m < 0$ we use this and eq. (A8) for the $b_{\ell m}$'s. It is straightforward to show that for a circular beam eq. (A11) reduces to the well known expression.

Using the reality condition on the beam, eq. (A8), one may show that the $\int_0^{2\pi} d\phi$ integral in eq. (A11) may be replaced by a $[1 + (-1)^{-m}] \int_0^\pi d\phi$ integral. Clearly, the $b_{\ell m}(\mathbf{x}'_3)$'s vanish for odd m .¹⁴ Since $f(\phi)$ is a function of $\sin^2(\phi)$, it is straightforward though tedious to show that the imaginary part of $e^{-im\phi}$ in eq. (A11) leads to an expression that vanishes. Thus we have

$$\begin{aligned} b_{\ell m}(\gamma_P) &= \frac{[1 + (-1)^{-m}](\ell)^{-m}}{\pi(\ell + 0.5)^{3/2}} \sqrt{\frac{(\ell+m)!}{(\ell-m)!}} \frac{1}{\sigma_1\sigma_2} \\ &\times \int_0^\pi d\phi \cos(m\phi) f^3(\phi) e^{-f^2(\phi)} [I_{(m-1)/2}(f^2(\phi)) - I_{(m+1)/2}(f^2(\phi))]. \end{aligned} \quad (\text{A13})$$

For an elliptical Gaussian beam function, this approximate semi-analytic spherical harmonic transform agrees well with the exact fully numerical transform.

¹⁴This is true provided the integral does not diverge. In fact it is straightforward to establish that it is integrable. We use $e^{im\phi} = \cos(m\phi) + i\sin(m\phi)$ and consider the real and imaginary parts separately. Both of these are continuous functions of ϕ over $0 < \phi < \pi$ and are thus Riemann integrable over this interval (see pp. 42 and 63 of Whittaker & Watson 1969).

REFERENCES

- Aghanim, N., Forni, O., & Bouchet, F.R. 2001, *A&A*, 365, 341
- Bond, J.R., & Efstathiou, G. 1987, *MNRAS*, 226, 655
- Bond, J.R., Jaffe, A.H., & Knox, L. 2000, *ApJ*, 533, 19
- Coble, K. 1999, Ph.D. thesis, University of Chicago
- Coble, K., et al. 1999, *ApJ*, 519, L5
- Dawson, K.S., Holzapfel, W.L., Carlstrom, J.E., Joy, M., LaRoque, S.J., & Reese, E.D. 2000, *ApJ*, submitted
- Dodelson, S. 2000, *Int. J. Mod. Phys. A*, 15, 2629
- Douspis, M., Bartlett, J.G., Blanchard, A., & Le Dour, M. 2001, *A&A*, 368, 1
- Fischler, W., Ratra, B., & Susskind, L. 1985, *Nucl. Phys. B*, 259, 730
- Ganga, K., Ratra, B., Gundersen, J.O., & Sugiyama, N. 1997, *ApJ*, 484, 7
- Ganga, K., Ratra, B., Lim, M.A., Sugiyama, N., & Tanaka, S.T. 1998, *ApJS*, 114, 165
- Ganga, K., Ratra, B., & Sugiyama, N. 1996, *ApJ*, 461, L61
- Gawiser, E., & Silk, J. 2000, *Phys. Rept.*, 333-334, 245
- Górski, K.M., Ratra, B., Stompor, R., Sugiyama, N., & Banday, A.J. 1998, *ApJS*, 114, 1
- Górski, K.M., Ratra, B., Sugiyama, N., & Banday, A.J. 1995, *ApJ*, 444, L65
- Gradshteyn, I.S., & Ryzhik, I.M. 1994, *Table of Integrals, Series, and Products*, ed. A. Jeffrey (San Diego: Academic)
- Knox, L. 1999, *Phys. Rev. D*, 60, 103516
- Knox, L., & Page, L. 2000, *Phys. Rev. Lett.*, 85, 1366
- Lineweaver, C.H. 2001, in *Gravitational Lensing: Recent Progress and Future Goals*, ed. T. Brian-
erd & C. Kochanek (Boston: Boston University Press), in press
- Mukherjee, P., Hobson, M.P., & Lasenby, A.N. 2000, *MNRAS*, 318, 1157
- Padin, S., et al. 2001, *ApJ*, 549, L1
- Park, C.-G., Park, C., Ratra, B., & Tegmark, M. 2001, *astro-ph/0102406*, *ApJ*, 556, in press
- Phillips, N.G., & Kogut, A. 2001, *ApJ*, 548, 540

- Podariu, S., Souradeep, T., Gott, J.R., Ratra, B., & Vogeley, M.S. 2001, astro-ph/0102264
- Ratra, B., Ganga, K., Sugiyama, N., Tucker, G.S., Griffin, G.S., Nguyêñ, H.T., & Peterson, J.B. 1998, *ApJ*, 505, 8
- Ratra, B., Stompor, R., Ganga, K., Rocha, G., Sugiyama, N., & Górski, K.M. 1999, *ApJ*, 517, 549
- Ratra, B., Sugiyama, N., Banday, A.J., & Górski, K.M. 1997, *ApJ*, 481, 22
- Rocha, G. 1999, in *Dark Matter in Astrophysics and Particle Physics* 1998, ed. H.V. Klapdor-Kleingrothaus & L. Baudis (Bristol: Institute of Physics Publishing), 238
- Rocha, G., Stompor, R., Ganga, K., Ratra, B., Platt, S.R., Sugiyama, N., & Górski, K.M. 1999, *ApJ*, 525, 1
- Romeo, G., Ali, S., Femenía, B., Limon, M., Piccirillo, L., Rebolo, R., Schaefer, R. 2001, *ApJ*, 548, L1
- Subrahmanyam, R., Kesteven, M.J., Ekers, R.D., Sinclair, M., & Silk, J. 2000, *MNRAS*, 315, 808
- Tegmark, M., & Zaldarriaga, M. 2000, *ApJ*, 544, 30
- Varshalovich, D.A., Moskalev, A.N., & Khersonskii, V.K. 1988, *Quantum Theory of Angular Momentum* (Singapore: World Scientific) (VMK)
- Whittaker, E.T., & Watson, G.N. 1969, *A Course of Modern Analysis* (New York: Cambridge University)
- Wu, J.-H.P., et al. 2001a, *ApJS*, 132, 1
- Wu, J.-H.P., et al. 2001b, astro-ph/0104248

FIGURE CAPTIONS

Fig. 1.— Contour plots of the zeroth order (eq. [22], left panel) and first order (eq. [23], right panel) terms in the non-circularity perturbation expansion of the flat-sky approximation elementary window function for an elliptical Gaussian beam function experiment. These are computed for the nominal FWHM beamwidths of the Python V experiment, 1.02° in elevation and 0.91° in azimuth. They are plotted as a function of dimensionless variables $k\mathbf{x}$, and the two panels are centered on the center of the zeroth order circular beam function window function. As expected, the flat-sky window function for the circular beam in the left panel is circularly symmetric. For a fixed value of k the first order correction in the right panel must be multiplied by $-k^2(\sigma_2^2 - \sigma_1^2)$ before being added to the zeroth order term. For Python V the higher order terms are small compared to the first order term and visually have roughly similar structure.

Fig. 2.— Coefficients $|b_{\ell m}(\mathbf{x}'_3) b_{\ell m'}(\mathbf{x}'_3)|$ of the six lowest order terms in the perturbation expansion of the Wigner method elementary window function (see eqs. [33] and [31]). These are computed for the elliptical Gaussian Python V beam function and are plotted as a function of $\ell\sigma_{\text{RMS}}$. For the Python V beam function the ellipticity parameter $\epsilon = 0.26$. Non-circularity corrections are important for $\ell\sigma_{\text{RMS}} > 1$. Note that the peak shifts to higher values of ℓ for higher order terms, relative to the peak position for lower order coefficients. The shape of the curves are independent of σ_{RMS} but depend sensitively on the beam function ellipticity.

Fig. 3.— Contour plots in the azimuth-declination plane (with azimuth along the horizontal axis) of terms in the Wigner method perturbation expansion of the elementary window function for the Python V experiment. These are plotted for multipole $\ell = 100$ such that $\ell\sigma_{\text{RMS}} \sim 1$. The left panel shows the zeroth order isotropic term $d_{00}^\ell(\gamma)$ and the right panel shows the first order correction term $\{\cos(2\alpha) + \cos(2\beta)\} d_{02}^\ell(\gamma)$ (see eq. [33]). Here γ is the angular separation between the central pixel and the pixel at the given azimuthal and declination sky coordinates.

Fig. 4.— Two sets of the eight equal-modulation exact Python V zero-lag complete window functions $W_\ell^{(m,m)}(\gamma, \gamma)$. The dark solid and light dotted curves correspond to window functions at the two extreme declinations $\delta = -63^\circ$ and -45.4° , respectively. Higher modulation window functions peak at progressively larger values of ℓ and with smaller amplitude. The dashed curve is the exact Python V zero-lag elementary window function at $\delta = -63^\circ$. Note that higher modulation complete window functions peak at ℓ a few times larger than the inverse beamwidth ($\sigma_{\text{RMS}}^{-1} \approx 140$) which is where the non-circularity corrections start to become important (see Fig. 2). For the same difference in azimuth the angular separation between two equal declination points ($\Delta\phi \cos \delta$) is smaller at larger $|\delta|$. Consequently, for the same modulation, the window function at $\delta = -63^\circ$ peaks at a larger multipole than the window function at $\delta = -45.4^\circ$.

Fig. 5.— Comparisons between Python V flat bandpower equal-modulation covariance matrix elements computed using different approximations. Plotted are the relative difference between $F_\ell^{(m,m)}(\gamma_i, \gamma_j)$ (eq. [41]) computed using an approximate window function and computed using the

exact window function, and normalized by dividing by the flat bandpower $C_{ij}^{(m,m)}$. The approximations considered are the circular beam approximation, (“wig00” in blue), the three successive leading improvements to this in the Wigner method perturbation expansion (“wig20” in green, “wig22” in red, and “wig40” in black, see eq. [33]; here each successive improvement includes all lower order terms), and the flat-sky approximation (“flat” in cyan). Two curves are shown for each approximation, those corresponding to modulation 2 (dashed) and 8 (solid). At large ℓ the modulation 8 curves converge to a lower accuracy than the corresponding modulation 2 curves because the non-circularity correction is more significant for higher modulations. Upper panels show differences for zero-lag covariance matrix elements at the two extreme declinations: *a*) $\delta = -63^\circ$ and *b*) $\delta = -45^\circ.4$. Lower panels show differences for non-zero-lag covariance matrix elements. Panel *c*) corresponds to pixels separated in azimuth by 20° at declination $\delta = -63^\circ$ and panel *d*) corresponds to two neighboring, equal azimuth, pixels at declinations $\delta = -63^\circ$ and -62° (in panel *d*) the solid red curve covers the solid black curve for $\ell \lesssim 300$). The flat-sky approximation fares well in all cases except for pixels separated in declination, where it fails even for small-separation pixel pairs, see panel *d*). Panel *d*) also shows the enormous improvement over the circular beam function approximation (wig00) achieved by accounting for even just the first order Wigner method correction (wig20). Panel *c*) highlights the need to compute to a large enough value of ℓ to achieve sufficient accuracy, e.g., truncating the circular beam function approximation (wig00) at intermediate ℓ leads to an inaccurate result.

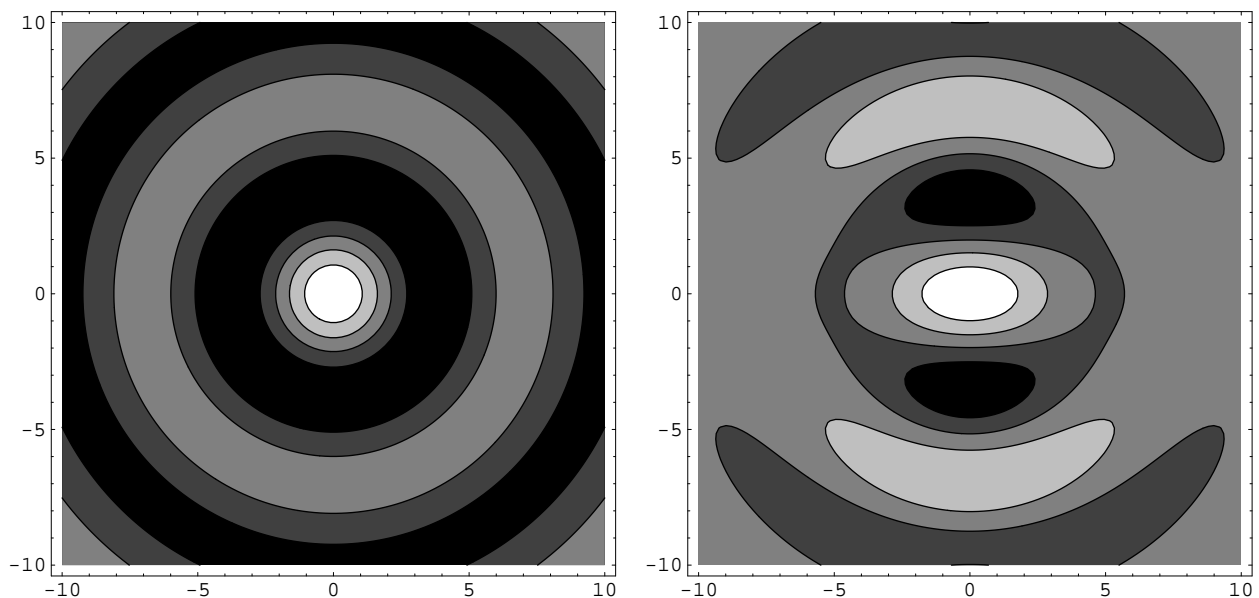


Figure 1

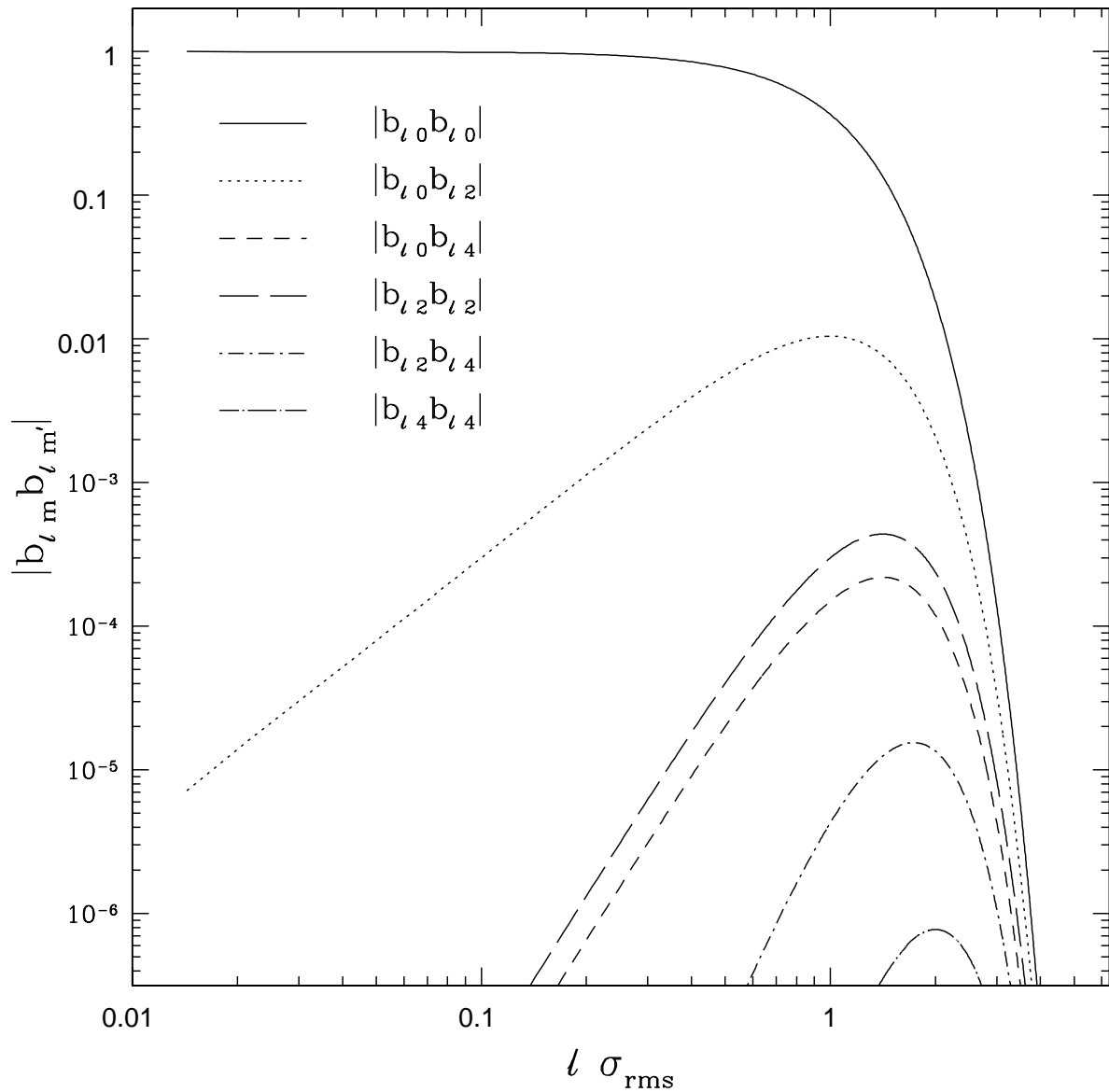


Figure 2

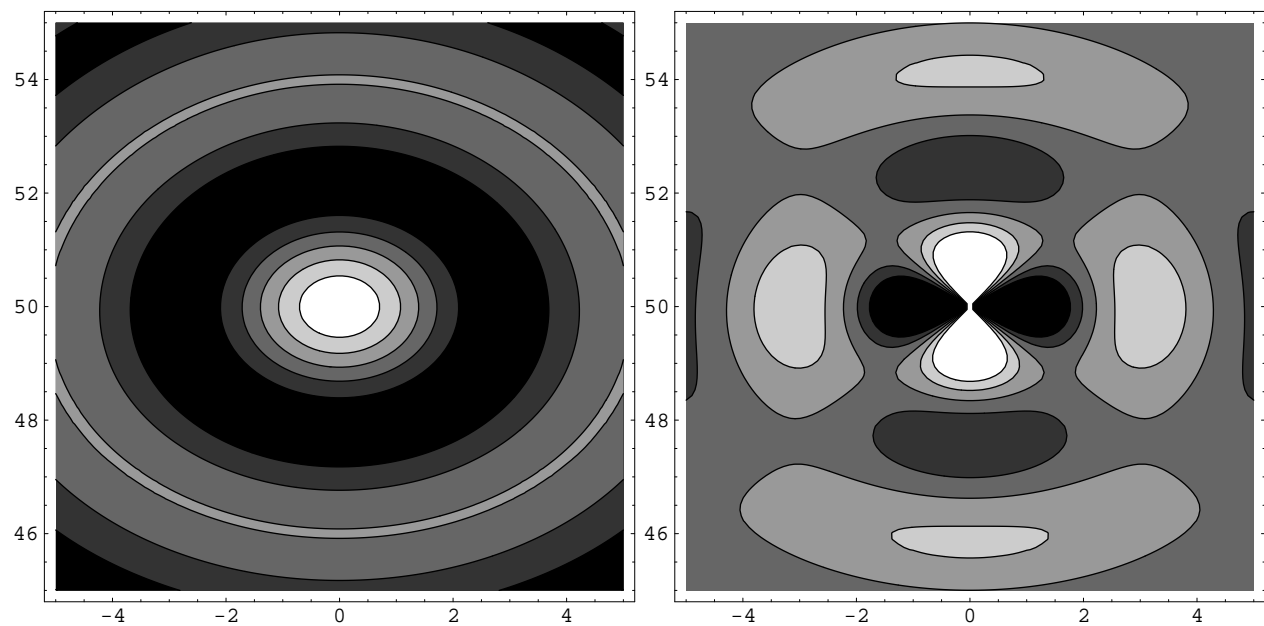


Figure 3

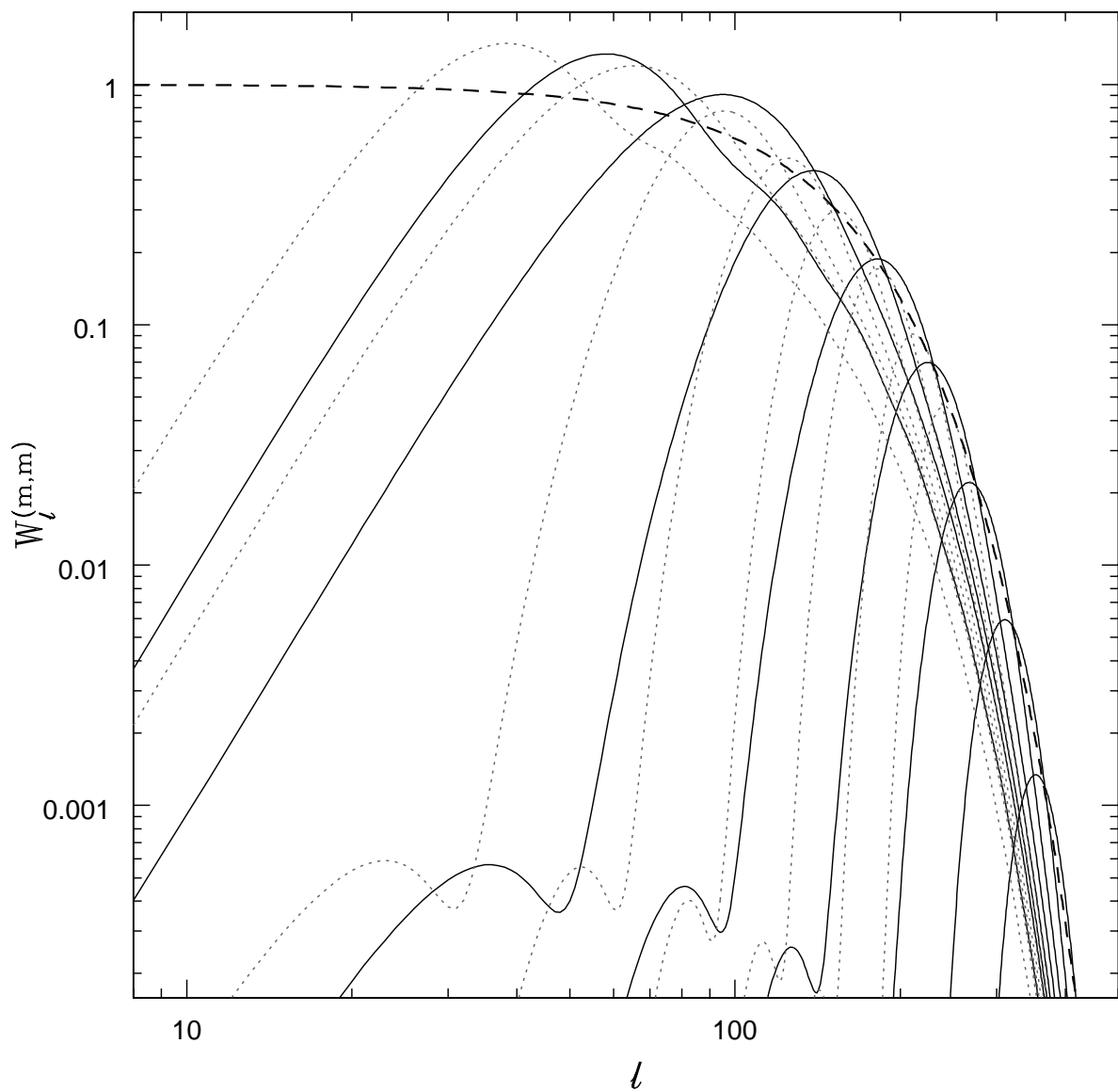


Figure 4

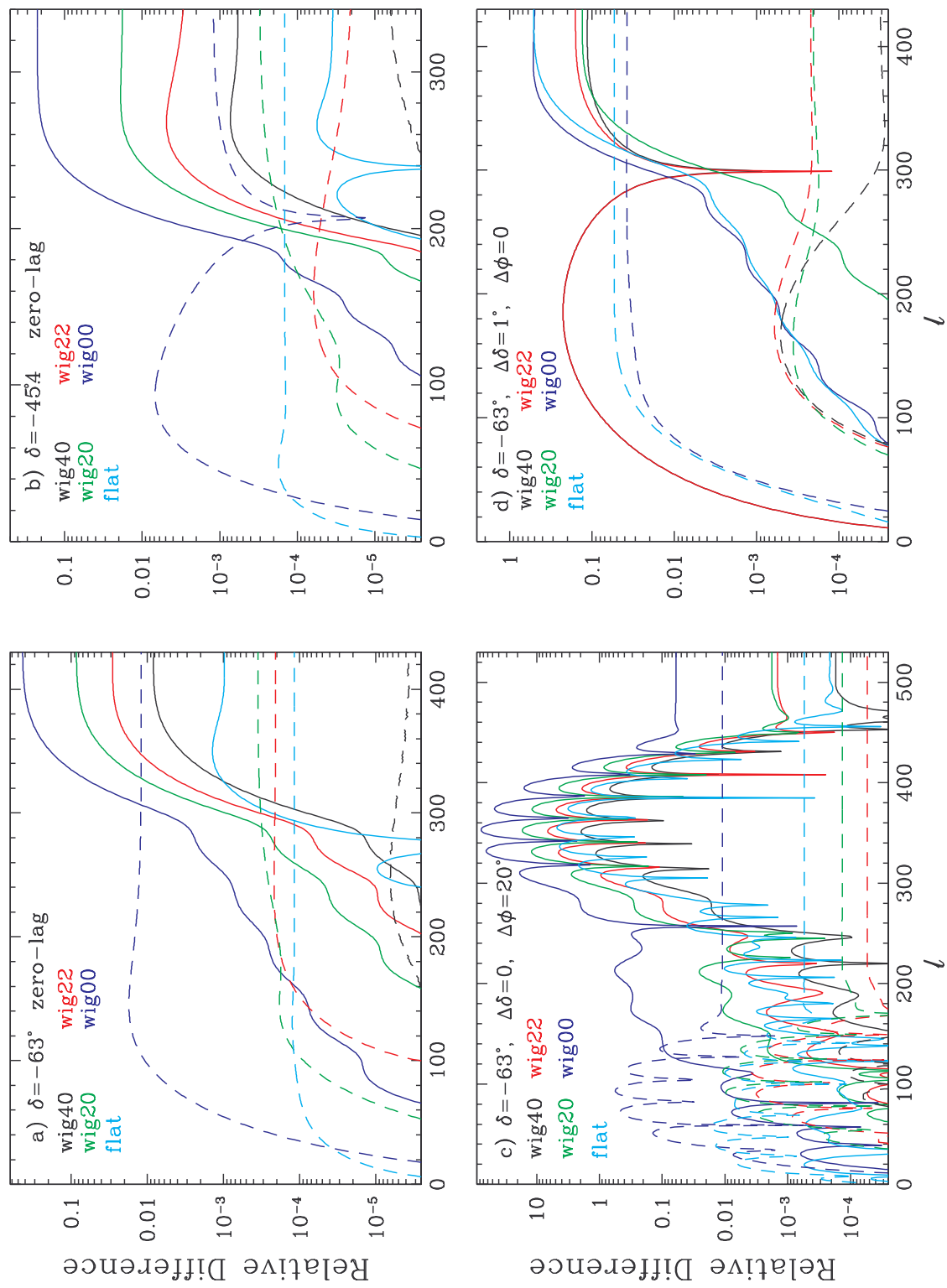


Figure 5